Supplementary Information: Micromechanics of cellularized biopolymer networks

Christopher A. R. Jones*, Matthew Cibula*, Jingchen Feng‡, Emma A. Krnacik† , David H. McIntyre*, Herbert Levine‡, Bo Sun*[1]

[1*] *Department of Physics, Oregon State University, Corvallis OR, 97331;* [‡] *Center of Theoretical Biophysics and Department of Bioengineering, Rice University, Houston, TX 77005;* [†] *Department of Biochemistry and Biophysics, Oregon State University, Corvallis OR, 97331*

Contents

S1: HOLOGRAPHIC OPTICAL TWEEZERS CALIBRATION

A holographic optical tweezers system with a 1064-nm trapping laser and a 100X, 1.6 NA, oil-immersion objective is used for micromechanical measurements. Video microscopy measurements are taken with the sample illuminated by a red LED and recorded at 60 fps, while the displaced trap is pulsed at 0.7 Hz by a mechanical shutter. To determine the location of the particle, the video microscopy images are analyzed with a tracking algorithm based on the radial symmetry of the particle's image [1]. The particle trajectories are then fitted using a built in pulse fitting function in MATLAB (MathWorks, Inc.) to obtain the mean displacements.

The micromechanical measurements described in the main text require precise control over the magnitude and direction of the applied trapping force. For small trap displacements, the force is approximated as linearly proportional to the displacement of the trap relative to the particle. We calculate the force in the direction of the trap as $F = k_t(d_t - \Delta d^{\parallel})$, where k_t is the stiffness of the trap, d_t is the displacement of the trap from the equilibrium position of the particle, and $\Delta d^{\parallel}$ is the displacement of the particle in the direction of the trap displacement. We carry out three calibration experiments, one to determine the stiffness of the trap, another to determine the appropriate trap displacement, and the final to test the precision of the direction of applied forces.

The stiffness of the trap is determined using the Equipartition method [2]. We trap a 3 μm particle in water and observe the Brownian motion due to thermal fluctuations. A video of the trapped particle is recorded at 60 frames per second for approximately 1 minute 30 seconds (roughly 5000 total frames). Fig S1A shows the Brownian motion of a typical particle. According the Equipartition theorem, the thermal energy is equal to the average potential energy of the particle with $\frac{1}{2}k_bT$ for each degree of freedom in the motion. Treating the optical trap as a harmonic potential well, we get $\frac{1}{2}k_bT = \frac{1}{2}k_t\langle x^2\rangle$, where k_b is the Boltzmann constant, T is the absolute temperature of the water, and $\langle x^2\rangle$ is the variance, or square of the standard deviation σ_x, of the spatial fluctuations ($\langle x\rangle = 0$). We seperate the Brownian motion into the x and y components and fit each with a Gaussian distribution to find the standard deviation. Fig. S1B shows a histogram of fluctuations in the x direction for a typical particle. The standard deviations for both directions are $\sigma_x = 31.3\ nm$ and $\sigma_y = 33.1\ nm$. Using an absolute temperature of 294 K, this gives

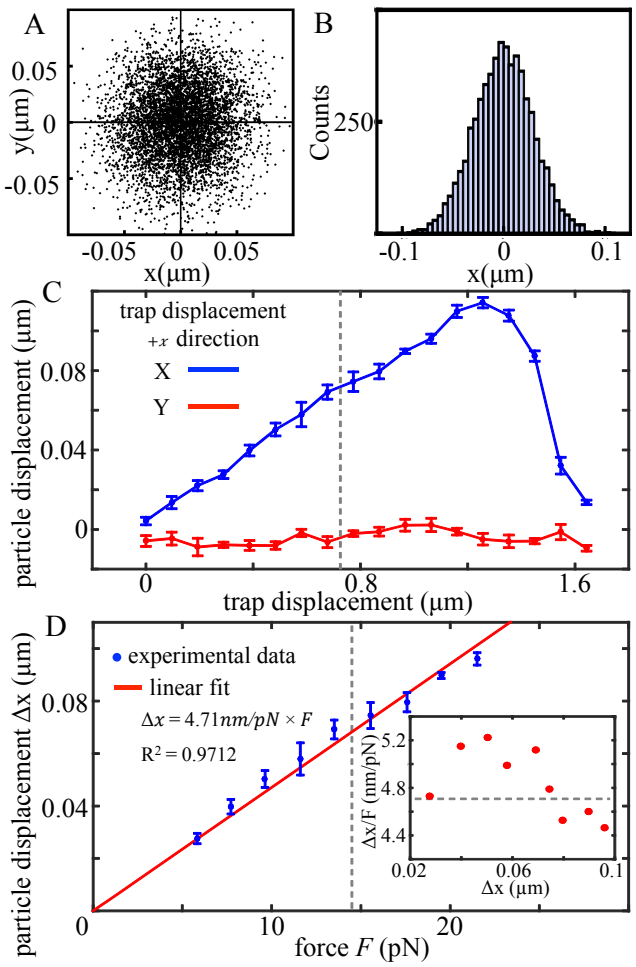

FIG. S1: Calibration of holographic optical trap stiffness and linearity of trapping force. (A) XY trajectory of the Brownian motion of a 3 μm diameter sphere trapped in water at 35% laser power. (B) Histogram of the x position of the particle showing a Gaussian distribution with a standard deviation of $\sigma_x = 0.0313 \mu m$. (C) Plot of particle dispacement vs. trap displacement for a 3 μm particle embedded in a homogeneous 1.5 mg/ml collagen gel. Trap is displaced in the $+x$ direction and the particle response is seperated into x and y displacement. The vertical dashed line represents a trap displacement of 0.725 μm which is the trap displacement used for all micromechanical measurements. (D) Plot of particle displacement vs. force with a linear fit passing through the origin. The vertical dashed line is at 14.5 pN, corresponding to a trap displacement of 0.725 μm. Inset: Plot of $\Delta x/F$ (inverse spring constant) vs. particle displacement. The horizontal line represents 4.71 $nm/\mu m$, the slope of the linear fit to the experimental data. Error bars in C and D represent standard deviation of particle displacements.

stiffnesses of $k_x = 4.159\ pN/\mu m$ and $k_y = 3.72\ pN/\mu m$. Finally, although micromechanical measurements were carried out at 60% laser power, this calibration was done at 35% power to increase the observed Brownian motion. This increase in power increases the intensity of the beam by a factor of 5.348, so rescaling the stiffnesses we get $k_x = 22.24\ pN/\mu m$ and $k_y = 19.98\ pN/\mu m$.

While the calibration was done in water, the micromechanical measurements were done in collagen gels. For the gels used in our experiments, collagen only makes less than 2% of the total mass while the rest is mainly water. Therefore we expect the trap stiffness in water and in collagen gels are very close. Indeed, from the recent turbidity data of collagen gel ($\sim$ 1 cm^{-1}[3]), we estimate that the scattering of light at 50 μm depth will cause less than 1% reduction in the trap stiffness in collagen gel.

To determine the appropriate trap displacement, we perform a calibration on particles embedded in a homogeneous collagen gel. We center the trap on the particle, then increase the trap displacement in the $+x$ direction in increments of 0.096 μm. The particle displacement as a function of trap displacement is plotted in Fig. S1C. The particle response increases roughly linearly until it reaches a maximum at a trap displacement of 1.35 μm. For our linear model of the trapping force to be valid, we chose a trap displacement of 0.725 μm for all micromechanical measurements, safely within the approximately linear region and represented by the vertical dashed line in Fig. S1C. Also, note that y displacements were minimal as a highly isotropic particle was chosen for this calibration.

Next we focus on the linear region of trap displacements to explore the linearity of collagen response. Fig. S1D shows particle displacement in the x direction Δx vs force F for trap displacements in the range 0.288 μm to 1.056 μm. F represents both the trapping force and the elastic force from the collagen which are equal in magnitude once the particle reaches its displaced position. We see that the particle displacement is quite linear with respect to force in this region and a linear fit to the experimental data is performed in MATLAB. The fit is restricted to pass through the origin and has a slope of 4.71 nm/pN ($R^2 = 0.9712$) which is the apparent inverse spring constant $\Delta x/F$ of the collagen around this particle. The dashed vertical line shows a force of 14.5 pN corresponding to a trap displacement of 0.725 μm. The inset of Fig. S1D shows $\Delta x/F$ for each different particle displacement with the horizontal line representing 4.71 nm/pN, the value obtained from the linear fit. The average difference between the individual $\Delta x/F$ and the fitted value is less than 5%. The

results suggest that for the range of particle displacements we used in our experiments, the micromechanics does not dependent on the probing force.

Finally, we calibrate the directional precision with which we can apply forces to particles embedded in collagen. Our holographic optical tweezers use a computer-controlled spatial light modulator to control the location of optical traps. The holograms are calculated in LabView using software based on 'Blue Tweezers' from the University of Glasgow [4] and allow precise control of trap position in real time. We carry out the calibration in water by calculating trap positions displaced by 0.725 μm from the center location at various angles. The trap position relative to the center is calculated using polar coordinates with $\rho = 0.725\ \mu m$ and φ defined as the angle counter clockwise from the $+x$ direction. We increase φ in 15° increments and compare the actual mean position of the particle with the calculated trap location. Fig. S2A compares the calculated and actual trap positions for all angles. Fig. S2B shows the difference $\delta\varphi$ between the actual trap angle and the expected

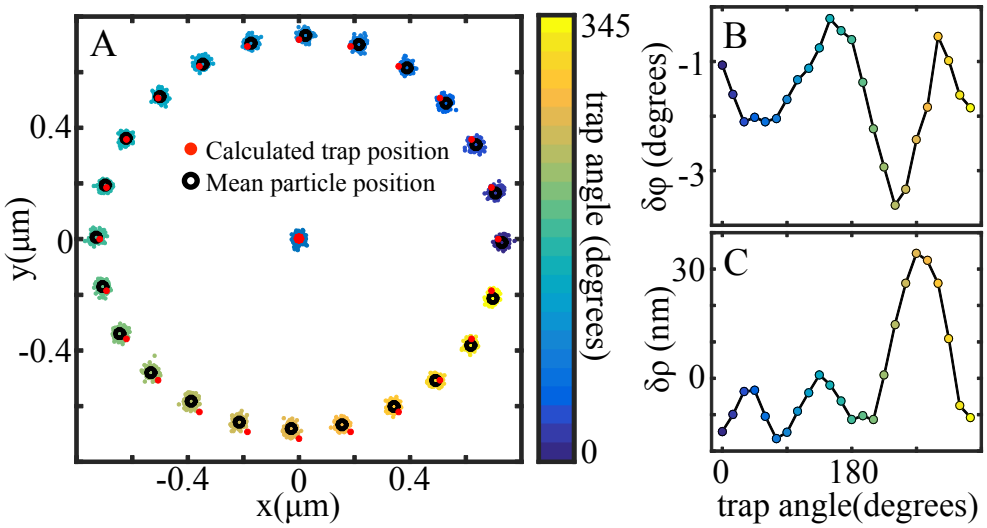

FIG. S2: Calibration of angular and radial precision of trap displacement with holographic optical tweezers. (A) XY trajectories of a particle trapped in water, with the center spot representing the undisplaced trap position and outer spots representing the trap displaced holographically at different angles around the center spot. The trap displacement angle φ is defined as the angle couterclockwise from the $+x$ direction. The trap angle is increased by 15° steps and the radial trap displacement ρ is 0.7250 μm. (B) Difference between trap angle and expected angle. (C) Difference between trap displacement and expected displacement.

angle. Overall, there is an average angular shift of -1.6° with a maximum difference of -3.6°. In addition, we compare the measured displacement ρ with the expected value of 0.725 μm and find a maximum difference of 35 nm. The difference $\delta\rho$ is plotted in Fig. S2C. Overall, we expect these small errors in the spatial precision of the trap location have a negligable effect on micromechanical measurement.

S2: MICROMECHANICS OF ADDITIONAL COLLAGEN GEL SAMPLES

Several other collagen gels were tested to confirm that the micromechanical trends presented in the main text are due to more than just sample to sample variation. Fig. S3 shows the results for two additional gels prepared with the exact same protocol as those presented in Fig. 2 and 3 of the main text: both have final collagen concentrations of 1.5 mg/ml, one was prepared with deionized water at 37°C ,and the other was prepared with growth medium at 21°C. Fig. S3A shows the normalized histograms of compliance with the homogeneous, high temperature gel on top and the heterogeneous, low temperature gel on the bottom. As described in the main text, the high temperature gel has a much tighter distribution of local compliance and the compliance is lower on average. The low temperature gel again shows a wide distribution of local compliances. Fig. S3 B and C also support the trend, with broader distributions of anisotropy and off-axis angle in the low temperature gel, and narrower distributions for the high temperature gel.

In addition, we also test gels formed with growth medium at 37°C which lead to struc-

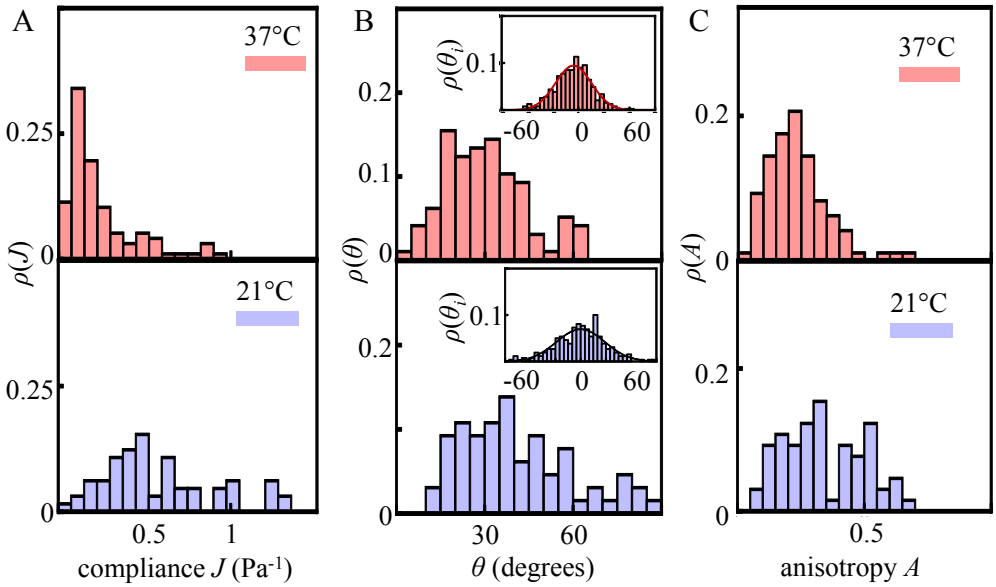

FIG. S3: Micromechanical measurement of two additional collagen gels. Plots on the left are for a sample prepared at 37°C in deionized water and plots on the right are for a sample prepared at 21°C in growth medium. (A) Normalized histogram for compliance J for both gels. (B) Normalized histograms for maximum off-axis angle θ. Insets shows directional off-axis angles θ_i for measurements in all four directions. (C) Normalized histograms for anisotropy A.

tural and mechanical properties different from either of the conditions described previously. The characterization of these conditions are particularly relevant because all cell-populated collagen samples are prepared with growth medium at 37°C. Fig. S4A shows confocal reflection images of two gels, one with and one without particles. Structurally, the collagen network has longer fibers than the high temperature DI water samples, but the fibers are still much shorter and more homogeneous than the low temperature gels. Fig. S4B-C show the results of micromechanical measurements, and again the properties are in between those of the previously described collagen samples. We see broader distributions and overall higher compliance, anisotropy, and off-axis angle than for the DI water sample. However, the results more closely resemble the low temperature growth medium gels than they do the DI water samples. Although the compliance, anisotropy, and off-axis angle are lower on average

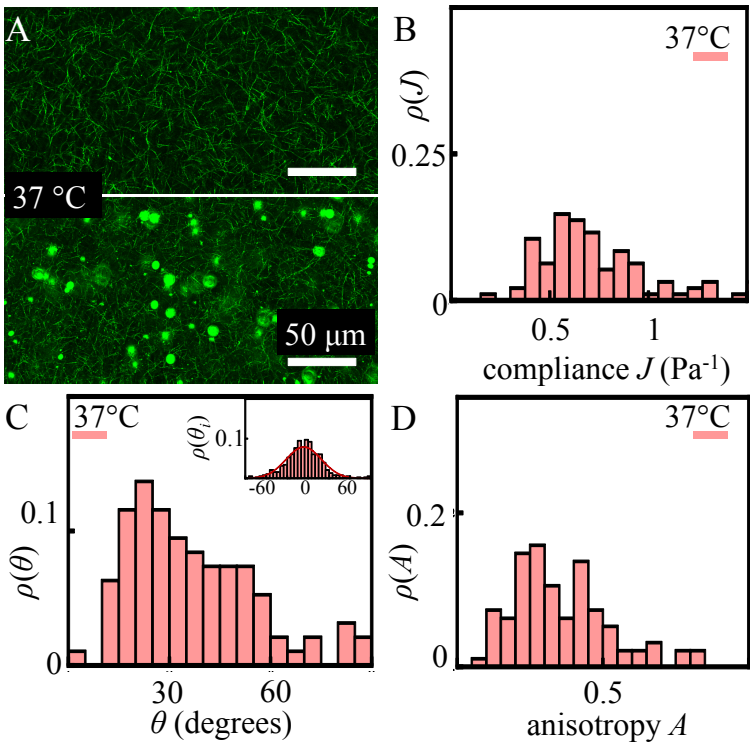

FIG. S4: A typical micromechanical measurement of collagen gel prepared at 37°C in growth medium at a concentration of 1.5 mg/ml. (A) Confocal reflectance image of two gels. Top gel is prepared without particles, bottom is prepared with 3 μm diameter particles. (B) Normalized histogram for compliance J. (C) Normalized histogram for maximum off-axis angle θ. Inset shows histogram of directional off-axis angles θ_i for measurements in all four directions. (D) Normalized histogram for anisotropy A.

for the high temperature gel, the distributions look very similar. It has been shown that in addition to temperature and pH, ionic strength during gelation also has a large effect on the structural and bulk mechanical properties of collagen gel [5]. Our results show higher similarity between gels prepared with growth medium at different temperature than those prepared at the same temperature with different solvents. This suggests that ionic strength during gelation also has a strong effect on the local micromechanics of collagen gel.

μ	CI of μ	σ	CI of σ	R^2	reference
-1.90	[-2.47, -0.310]	13.3	[10.3, 12.0]	0.98	Fig. 2, 37 °C
0.498	[-2.28, 3.56]	25.0	[21.2, 26.0]	0.96	Fig. 2, 21 °C
-5.77	[-6.68, -3.00]	21.1	[18.7, 21.7]	0.98	Fig. S3, 37 °C
-0.0770	[-1.53, 5.75]	28.7	[24.1, 30.1]	0.94	Fig. S3, 21 °C
-6.33	[-7.31, -4.03]	25.3	[20.6, 33.3]	0.98	Fig. S4

TABLE I: The normalized histograms of directional off-axis angles (θ_i) in all samples can be fit well with a Gaussian distribution $\rho(x) = \frac{1}{\sigma\sqrt{2\pi}} e^{-\frac{(x-\mu)^2}{2\sigma^2}}$ with mean μ and standard deviation σ. The table summarizes the fitting parameters, confidence intervals (CI, 95 %) as well as the goodness of fit (R^2).

S3: THREE DIMENSIONAL PARTICLE TRACKING

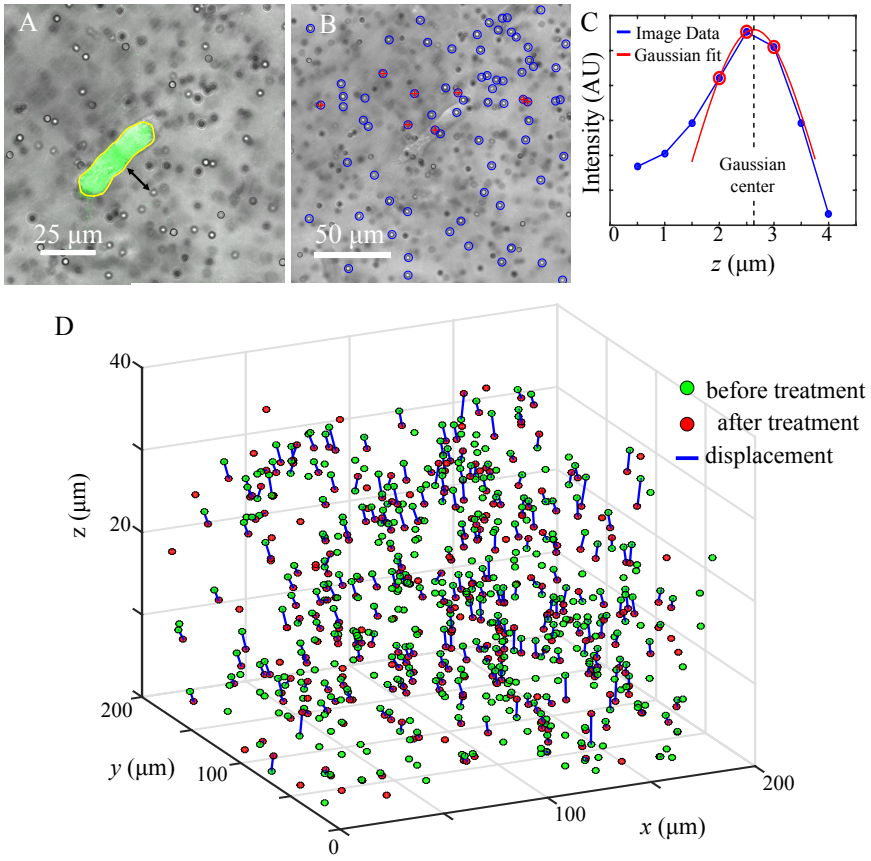

FIG. S5: 3D particle tracking to measure the strain field. (A) Overlay of non-descanned (NDS) and fluorescent channels of a confocal slice. The arrowed line represents the distance between a probe particle to the cell. (B-C) Example of 3D particle localization from the confocal image stack. (B) X-Y positions are first determined at subpixel resolution (blue circles). (C) The z position of a particle is determined by fitting the particle intensity profile $I(z)$ (blue curve) with a Gaussian function (red). Only three points around the maximum of $I(z)$ are included in the fitting, and z position of the particle is defined as the center of the Gaussian function. Red crosses in (B) indicate particles whose rounded z-position is in the shown confocal slice. (D) Deformation field obtained by associating 3D particle centers before and after cytochalasin D treatment.

In order to measure the 3D strain field caused by the cell contraction forces, we obtain confocal image stacks before and after cells are treated by cytochalasin D and utilize the non-descanned (NDS) channel (Fig. S5A). To determine the 3D particle centers, we first

determine the 2-D particle centers in all image slices, together with the integrated intensity associated with each 2-D particle center (Fig. S5B, [6]). The result of this step can be labeled as $S_i = [x_i, y_i, z_i, I_i]$, where z_i is an integer number (slice number) times the scanning step (0.5 μm). x_i, y_i, I_i are the coordinates and integrated intensity of 2D particle centers [7] which are detected in the slice corresponding to z_i, and i is the index of all 2D particle centers in all z-slices. Fig. S5B shows a typical image slice with its corresponding 2D centers labeled with blue circles. Since the same particle will appear in several consecutive slices, we then search in the collection $\{S_i\}$ that belong to the same particle. To do this, we notice that 2D projection of particle-to-particle distance is more than 10 pixels (1.7 μm) in all our samples, while the errors in 2-D particle locations is less than 0.5 pixels [7]. Therefore we consider S_i and S_j belong to the same group if

$$\sqrt{(x_i - x_j)^2 + (y_i - y_j)^2} < 0.34 \ \mu\text{m}, |z_i - z_j| < 0.4 \ \mu\text{m} \tag{1}$$

We have checked the effectiveness of these criteria by visually inspecting the image slices. We have confirmed that each group of $\{S_i\}$ corresponds to exactly one particle in the gel. Now to determine the actual 3D center $[X_\alpha, Y_\alpha, Z_\alpha]$ of particle α, consider its corresponding group $\{S_i\}$, $i \in \alpha$. We use the weighted average to calculate $X_\alpha = \frac{\sum_{i\in\alpha} x_i I_i}{\sum_{i\in\alpha} I_i}$, $Y_\alpha = \frac{\sum_{i\in\alpha} y_i I_i}{\sum_{i\in\alpha} I_i}$. To determine Z_α, note that the intensity profile along z direction $I(z) = I_i(z_i)$, $i \in \alpha$ has a characteristic bell shape (Fig. S5C). We fit the three points around the maximum of the intensity profile $I(z)$ with a Gaussian function and determine Z_α to be the center of the Gaussian fitting (Fig. S5D). Such three-point Gaussian fitting has been widely used in particle image velocimetry to obtain sub-pixel (less than 0.5 μm in our case) resolutions [8].

Using the above method, we determine the 3D particle centers before and after cytochalasin D treatment. We then apply the Crocker-Grier algorithm [7], which associates the 3D particle centers before and after cytochalasin D treatment (Fig. S5D), therefore obtaining the deformation field $\mathbf{D}(\mathbf{r})$ sampled at all the 3D particle centers. To further calculate the strain field ϵ_{ij}, we will need to calculate the numerical derivatives $\epsilon_{ij} = \frac{1}{2}(\frac{\partial \mathbf{D}i}{\partial r_j} + \frac{\partial \mathbf{D}j}{\partial r_i})$, where i, j label 3D spatial dimensions. To this end, we first interpolated the deformation field onto a fine regular grid lattice (grid spacing 0.17 μm) using natural neighbor interpolation [9], which provides a C^1 smooth approximation of $\mathbf{D}(\mathbf{r})$. We then take direct numeric derivatives on the regular grid to obtain the approximated ϵ_{ij}.

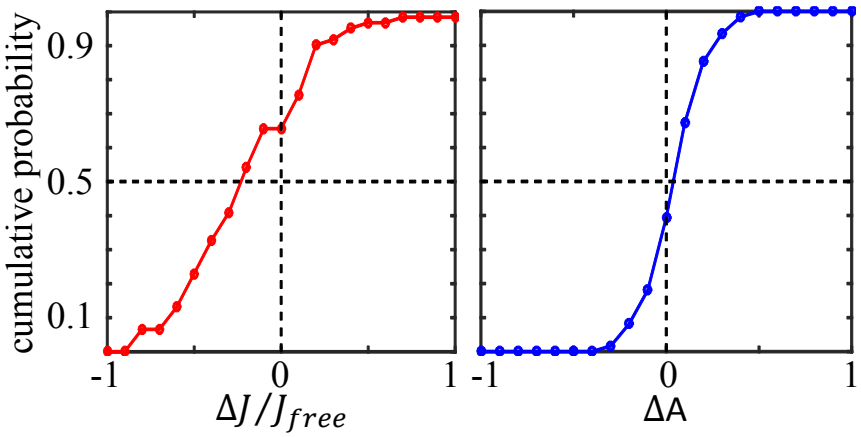

FIG. S6: Cumulative probability of changes in micromechancs caused by cellular traction forces. Left: cumulative probability of $\frac{\Delta J}{J_{free}}$, about 65% probing particles register decrease of local compliance. Right: cumulative probability of ΔA, about 38% probing particles register decrease of local anisotropy.

S4: SIMULATION OF MICROMECHANICAL MEASUREMENTS

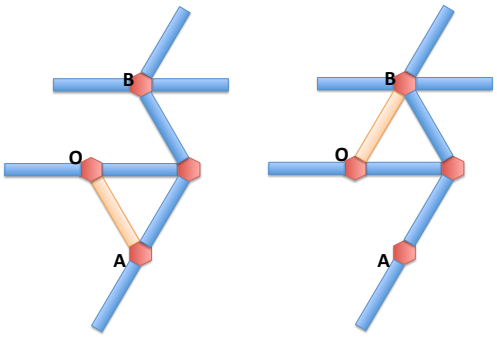

FIG. S7: Two examples of local network topology. Left: original local topology Right: local topology after changing one bond in node O.

To get the equilibrium configuration of the network, we apply conjugate gradient method to minimize the Hamiltonian. (Fig 5(a) in main text gives an example) We could further measure micro mechanics with exactly the same method used in experiment:

$$J = \frac{1}{4}\sum_i J_i \tag{2}$$

$$J_i = 6\pi a \frac{\Delta d_i^{\|}}{F_i^{\|}} \tag{3}$$

$$F_i^{\|} = k_t(d_t - \Delta d_i^{\|}) \tag{4}$$

Note that we use an arbitrary unit for compliance, while the units for anisotropy and mismatch angles are the same as those calculated from experimental data.

To construct the network, we first define the free energy.

$$FreeEnergy = -\sum_i K\alpha^{S_i} \tag{5}$$

Where K, α are two constants, S_i is the number of bonds of Node i. When $\alpha > 1$ and $K > 0$, nonuniform distribution gives lower energy (Note when all bonds form a huge cluster, free energy will reach minimum value).

The algorithm for constructing the network described in the main text naturally creates a homogenous network. Here we apply the metropolis algorithm to construct heterogeneous networks. By varying the value of parameters, networks with different heterogeneity can be built. Here is how this algorithm works:

• Construct an uniform network
• Randomly choose a Node N_i and a bond B_j connecting to N_i
• Attempt to replace B_j with B_k, which is also connected to Node N_i (An example is shown in Fig. S7)
• Compute energy change ΔE due to previous step. (Note in Fig. 1. Only the number of bonds in node A and node B has been changed)
• If $\Delta E < 0$, accept the trial
• If $\Delta E > 0$, accept the trial with probability $p = exp(-\Delta E/T)$. Here T is an effective temperature
• Go to second step, unless maximum number of iterations is reached.

We can construct networks with different heterogeneity by varying temperature T. (See Fig. S8 for examples)

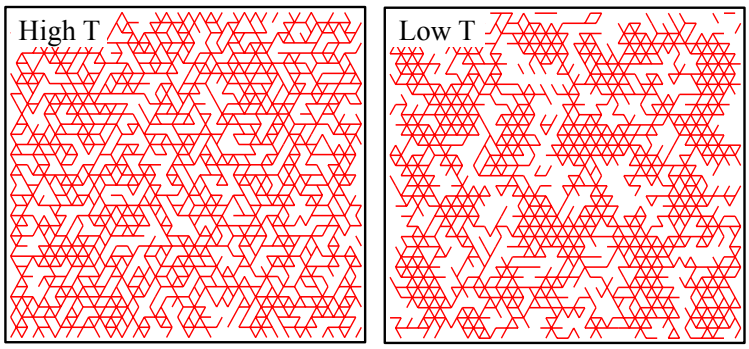

FIG. S8: Two examples of network topology. Left: Network under high effective temperature Right: Network under low effective temperature; these temperatures are not supposed to refer to the actual temperature in the collagen preparation but just as a phenomenological parameter which we can use to generate different types of networks

We can also generate spatial distributions of micromechanical properties, similar to those shown in Fig 3 of the main text. As we have pointed out, the value of anisotropy is uncertain at some points where the bead moves freely. Due to this reason, anisotropy is undefined at those points. Hence we only plot spatial maps of mismatch angles and compliance. (Fig. S9) Clearly, Fig. S9 shows qualitative differences between homogenous networks and heterogeneous networks.

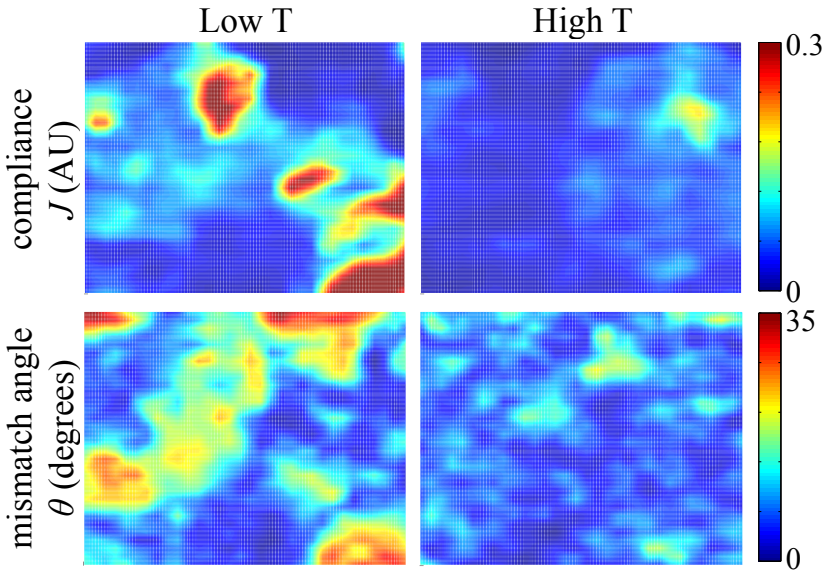

FIG. S9: Comparison of results between a homogeneous network and a heterogeneous network. Left: a heterogeneous network generated at a low effective temperature. Right: a homogeneous network generated with high effective temperature. For both networks, compliance is on the top and mismatch angle is on the bottom.

S5: SIMULATION OF CELLULARIZED ECM NETWORK

In our simulation, we relax the cell contraction force by moving the nodes on the ellipse boundary to their relaxation location. We further fix all nodes on the ellipse boundary to represent the rigidity of the cell. To see if cells suppress the local change of compliance for regions close to the cell, we delete the cell by allowing nodes on ellipse boundary to move freely. The new local compliance decreases monotonically as we increase r, which is qualitatively different from the previous result with a cell. Such a difference supports that cells suppress the local change of compliance for small r.

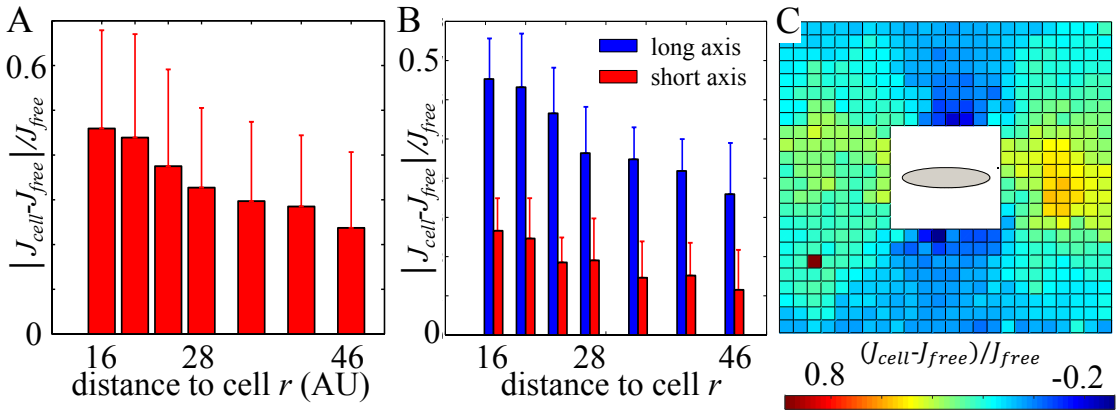

FIG. S10: The local change of compliance will monotonically decrease as r increases after removing the cell. A: The local change of compliance versus r, averaging over all directions. B: The local change of compliance versus r in long axis and short axis direction. Long axis direction is represented by the blue histograms and short axis direction is represented by the red histograms. C: Spatial map of the change of compliance ($\frac{\Delta J}{J_{free}}$) near a contracting cell. Fixed boundary condition is applied and it has been tested the decay of the relative change of compliance is not due to this boundary condition.

1. Parthasarathy R (2012) Rapid, accurate particle tracking by calculation of radial symmetry centers. *Nat. Methods* 9(7):724-726.
2. Brouhard G, Schek H, Hunt A (2003) Advanced optical tweezers for the study of cellular and molecular biomechanics. *IEEE Trans Biomed Eng* 50(1):121-125.
3. Zhu J, Kaufman LJ (2014) Collagen I self-assembly: revealing the developing structures that generate turbidity *Biophys. J.* 106(8):1822-1831.
4. Leach J et. al. (2006) Interactive approach to optical tweezers control. *Applied Optics* 45(5):897-903.
5. Achilli M, Mantovani D (2010) Tailoring mechanical properties of collagen-based scaffolds for vascular tissue engineering: the effects of pH, temperature and ionic strength on gelation. *Polymers* 2(4):664-680.
6. Pelletier V, Gal N, Fournier P Kilfoil ML (2009) Microrheology of Microtubule Solutions and Actin-Microtubule Composite Networks. *Phys. Rev. Lett* 102:188303-188306.

7. Crocker JC, Grier, DG (1996) Methods of Digital Video Microscopy for Colloidal Studies. *J. Colloid Interface Sci.* 179:298-310.
8. Thielicke, W, Stamhuis, EJ (2014) PIVlab V Towards User-friendly, Affordable and Accurate Digital Particle Image Velocimetry in MATLAB *J. Open Res. Software* 2(1):e30.
9. Barnett V, Interpreting Multivariate Data (1981), chapter 2 (Wiley)